Earth and Space Science

RESEARCH ARTICLE
10.1029/2024EA003711

Special Collection:
Recent Advances on Modelling and Observations in Space and Earth Sciences

Thermal Infrared Spectrometers for the Polar Radiant Energy in the Far-Infrared Experiment (PREFIRE)

Brian J. Drouin[1], Tristan L'Ecuyer[2], Sharmila Padmanabhan[1], Marc Foote[1], Rudi Bendig[1], Simon Calcutt[3], Gary Hawkins[3], Harrison Herzog[1], Eric Hochberg[1], Matthew Kenyon[1], Giacomo Mariani[1], David A. Martinez[1], James McGuire[1], Ian Mckinley[1], Aronne Merrelli[4], Deacon Nemchick[1], Nasrat Raouf[1], Gary Spiers[1], and Daniel Wilson[1]

[1]Jet Propulsion Laboratory, California Institute of Technology, Pasadena, CA, USA, [2]University of Wisconsin, Madison, WI, USA, [3]University of Oxford, Oxford, UK, [4]Department of Climate and Space Sciences and Engineering, University of Michigan, Ann Arbor, MI, USA

Key Points:

- Instrumentation for low-cost, broad-band spectral thermal imaging has been developed for spaceflight
- Thermal radiances across the majority of the Planck function can be quantified in a single polychromatic imager
- We are poised to disentangle biases in polar radiometric processes to improve predictive capabilities of local and global climate models

Supporting Information:

Supporting Information may be found in the online version of this article.

Correspondence to:

B. J. Drouin,
brian.j.drouin@jpl.nasa.gov

Citation:

Drouin, B. J., L'Ecuyer, T., Padmanabhan, S., Foote, M., Bendig, R., Calcutt, S., et al. (2025). Thermal infrared spectrometers for the polar radiant energy in the far-infrared experiment (PREFIRE). *Earth and Space Science*, *12*, e2024EA003711. https://doi.org/10.1029/2024EA003711

Received 9 MAY 2024
Accepted 4 SEP 2025

Author Contributions:

Conceptualization: Brian J. Drouin, Tristan L'Ecuyer, Eric Hochberg, Matthew Kenyon, James McGuire, Aronne Merrelli, Daniel Wilson
Data curation: Brian J. Drouin, Rudi Bendig

Abstract The Polar Radiant Energy in the Far-InfraRed Experiment (PREFIRE) was selected by NASA to fly two miniaturized Thermal InfraRed Spectrometers (TIRS) capable of distinguishing the spectral signatures of surface and atmospheric properties in Earth's polar regions. A trade study examining spectral sampling as well as separation of cloudy and clear scenery at 20 km scales highlighted the possibility to utilize ambient (uncooled) detector technologies in a miniaturized spectrometer that could facilitate low-cost and rapid access to space. This work describes the design, implementation, testing and performance of two TIRS systems, as well as the challenges and acceptable limitations of the cost-constrained effort, that feature the novel joining of compact thermopile array technologies with concentric imaging spectrometry methods. The TIRS systems presented here each have 2.7 kg mass, draw 4.3 W power, and provide spectral resolution of 1.71 μm below 35 μm sampled at 0.86 μm increments.

Plain Language Summary Earth absorbs energy emitted by the Sun, radiating some of that as heat back into space. The energy exchange between Earth and space drives weather and climate. Scientists measure and track this energy using satellite instruments that can identify which parts of Earth's surface and atmosphere emit specific portions of the overall heat radiated into space. But these instruments are complicated and expensive, and until now, no one has built a sensor that can look at and separate all of Earth's heat emissions in a systematic way. The Polar Radiant Energy in the Far-InfraRed Experiment (PREFIRE) has developed a novel instrument that combines simple, miniaturized heat sensors with specially shaped optics and microelectronics to provide such measurements to further our understanding of the planet's weather and climate. Furthermore, implementation of the sensors has been done within a cost-capped mission profile that encourages development of a sustainable sensor system for Earth monitoring. This manuscript describes the instrument design, including its components and their characteristics, the system and its functionality, its trade-offs, cost limitations, and testing and performance information. PREFIRE began operating two of these instruments in space in 2024, in order to start quantifying the heat exchange processes in Earth's polar regions.

1. Introduction

The Arctic is changing more rapidly than anywhere else on Earth owing to unique feedbacks that locally amplify the effects of globally increasing greenhouse gas concentrations. These changes have far reaching societal implications that include increased vulnerability of local populations and ecosystems, new concerns for national security, and rising global sea levels caused by melting ice sheets. Yet projections of Arctic responses to increased CO_2 concentrations exhibit wide spreads that impede efforts to develop appropriate adaptation policies and mitigation strategies. For example, projections of the extent of September sea ice in 2050 under the IPCC RCP4.5 scenario vary by a factor of five across the models that contributed to the Fifth Assessment Report. Likewise, there is a factor of four spread in projected Greenland surface air temperatures and associated ice sheet melt contribution in the 1.1 mm yr^{-1} range to global sea level rise from 2080 to 2099. As a result, NASA and other agencies desire improved predictions of the consequences of Arctic climate change as a national priority.

The poles play a critical role in regulating Earth's climate, acting as a thermostat by radiating 1.2 PetaWatts (10^{15} Watts) of excess energy absorbed at lower latitudes to space. This, coupled to the ongoing rapid (and variable) trends in arctic sea ice and snow cover, has impacts globally. Accurate estimates of Arctic energy fluxes and their response to cloud cover, sea ice cover, and land-surface characteristics are, therefore, essential to modeling current and future climate.

The relative balances between upwelling and downwelling radiative fluxes at the surface are highly uncertain due to strong spectral modulations by water vapor, clouds and surfaces, that have not been thoroughly characterized across the entire longwave infrared. It has been hypothesized that feedbacks involving the longwave portion of the energy budget may significantly influence Arctic amplification by reducing the efficacy of the Arctic thermostat. Indeed, amplified surface energy imbalances owing to an enhanced Arctic greenhouse effect may exceed those caused by the reduced albedo that results from sea ice loss. Furthermore, it has been suggested that these feedbacks are the strongest drivers of ice sheet melt rates and, by extension, sea level rise (Henderson et al., 2021; Hwang et al., 2011). With the ever-increasing attention on Arctic climate change and its geopolitical, ecological, and societal implications, there is an urgent need to resolve outstanding questions concerning the magnitude and impacts of longwave radiative feedbacks in this region.

Through spectrally resolved observations of radiances spanning the radiatively significant portions of the mid- and Far InfraRed (FIR), PREFIRE data will be utilized to improve earth system and ice-sheet models and are expected to reduce uncertainty in future climate scenario predictions. In order to implement this project rapidly and within the broad scope of NASA earth science, the project was proposed and selected within the cost capped Earth Ventures Instrument program. This program supports the development, launch and operation of free-flying cubesats with science payloads. PREFIRE (L'Ecuyer et al., 2021) is now flying two 6U CubeSat spacecraft at 98° inclination, 525 km altitude orbits, in two different node crossings (± 2 hr from terminator) (B. J. Drouin et al., 2022); each with a miniaturized IR spectrometer, covering the 5–54 μm spectral region at 0.8 μm spectral sampling, operating for one seasonal cycle (a year) with diurnal subsampling.

2. Spectroradiometric Thermal Imaging

Sensing of emission from the top-of-the-atmosphere has well founded theoretical basis that is useful for quantifying spectral radiances over the geophysical state space covered by a spectroradiometric imager such as the TIRS. We provide here an overview of the theory in order to implement a quantitative instrument model based on the components, system, and test data outlined in the following sections. This culminates in a discussion of data sufficiencies and error budgets that are useful to define the performance of the instrument and set expectations for science.

The signals of interest originate as emission from the Earth surface or atmosphere, depending on the concentrations of infrared absorbing molecules and the distribution of clouds. Spectral deviations from ideal blackbody behavior will be characterized, classified and quantified by surface and cloud type. The signal level from the observed Earth scene can be expressed as a function of scene temperature, T_{sc}, with the Planck function:

$$B_\lambda(T_{sc}) = \frac{2hc^2}{\lambda^5}\frac{1}{e^{\frac{hc}{\lambda kT_{sc}}}-1} \tag{1}$$

In which B_λ is the spectral radiance of a blackbody, in $\mathrm{Wsr^{-1}\ m^{-2}\ \mu m^{-1}}$, h is Planck's constant in $\mathrm{Ws^2}$ and c is the speed of light in $\mathrm{ms^{-1}}$. The scene subscript sc refers both to the observed Earth scene, as well as the subscript denoting the cross-track field of view of the TIRS spectrometer. In general, the scene temperature in this case would have wavelength dependence (the brightness temperature spectrum of the scene). Alternately, B_λ could be defined directly by a radiative transfer model (Xie et al., 2022) with spectrally varying surface emissivity gas absorption, and emission or scattering due to aerosol and/or cloud layers. The spectral irradiance, I, in $\mathrm{Wm^{-2}}$, of a scene, per wavelength, $I_{sc,\lambda}$, in $\mathrm{Wm^{-2}\ m^{-1}}$, over a given wavelength range and field-of-view, is given by integrating the radiance over the wavelength interval and the angular coordinates:

$$I_{sc,n} = \int_{\lambda_n}^{\lambda_{n+1}} \delta\lambda \int_{\Omega} \delta\alpha\delta\beta B_\lambda(T_{sc}) \cos\beta \sin\beta \tag{2}$$

in which the solid angle, A_Ω, results from the integration over the angles α, β. (A_Ω = Solid angle of the optics = $\pi \sin^2(\tan^{-1}(1/2f\#))$ (sr)). Note that simply integrating over the wavelength, and not the solid angle results in the

Formal analysis: Brian J. Drouin, Gary Hawkins, Harrison Herzog, Giacomo Mariani, David A. Martinez, James McGuire, Ian Mckinley, Gary Spiers, Daniel Wilson
Funding acquisition: Brian J. Drouin, Tristan L'Ecuyer, James McGuire, Aronne Merrelli, Nasrat Raouf, Daniel Wilson
Investigation: Brian J. Drouin, Sharmila Padmanabhan, Marc Foote, Simon Calcutt, Harrison Herzog, Ian Mckinley, Daniel Wilson
Methodology: Brian J. Drouin, Sharmila Padmanabhan, Marc Foote, Rudi Bendig, Simon Calcutt, Gary Hawkins, Eric Hochberg, Matthew Kenyon, David A. Martinez, James McGuire, Ian Mckinley, Aronne Merrelli, Deacon Nemchick, Nasrat Raouf, Gary Spiers, Daniel Wilson
Project administration: Brian J. Drouin, Tristan L'Ecuyer, Sharmila Padmanabhan, Simon Calcutt, Nasrat Raouf
Resources: Brian J. Drouin, Simon Calcutt, Gary Hawkins, Matthew Kenyon, Giacomo Mariani, James McGuire, Nasrat Raouf, Gary Spiers, Daniel Wilson
Software: Brian J. Drouin, Rudi Bendig, Deacon Nemchick, Daniel Wilson
Supervision: Brian J. Drouin, Sharmila Padmanabhan, Marc Foote, Giacomo Mariani, James McGuire, Daniel Wilson
Validation: Brian J. Drouin, Marc Foote, Harrison Herzog, Matthew Kenyon, David A. Martinez, James McGuire, Ian Mckinley, Deacon Nemchick, Daniel Wilson
Visualization: Brian J. Drouin, David A. Martinez, James McGuire, Ian Mckinley, Aronne Merrelli, Daniel Wilson
Writing – original draft: Brian J. Drouin, Tristan L'Ecuyer, Marc Foote, Gary Hawkins
Writing – review & editing: Brian J. Drouin, Gary Hawkins, Aronne Merrelli

spectral radiance, $L_{sc,n}$ that will be used as a retrieved data product. Here the subscript n refers to the wavelength interval spanning λ_{n+1}-λ_n, which may be labeled by its central (design) wavelength. When the angles are integrated over a hemisphere (2π steradians, where $\alpha^{\pm} = \pm\pi$ and $\beta^{\pm} = 0, \pi/2$) and all wavelengths are considered, the power is determined by the scene temperature and the Stefan-Boltzmann constant σ_B.

The 64 × 8 thermopile detector array in PREFIRE is situated behind optics with (a) a slit width that is chosen to be 2 pixel widths (l_d) in the spectral dimension, (b) a solid angle, A_Ω, determined by the optics. A novel feature of TIRS is that non-dispersive light is intentionally detected in a broad-band channel that corresponds to signals $I_{sc,0}$ determined primarily by the scene temperatures. The angular response of the system in the spectral direction is the convolution of the angular extent of the slit, the angular diffraction pattern, and the angular extent of the detector.

$$\mathfrak{R}_{n,\lambda} = \mathfrak{R}_{\text{slit}}(x' \pm l_{\text{sw}}/2) \otimes \mathfrak{R}_{\text{det}}(x_0 + l[n \pm 1/2]) \otimes \mathfrak{R}_{\text{diff}}(x, \lambda) \tag{3}$$

Here, $\mathfrak{R}_{n,\lambda}$ is the linearized response of the system in the spectral direction, $\mathfrak{R}_{\text{slit}}$ is the rectangular response function representing the slit, $\mathfrak{R}_{\text{det}}$ is the rectangular response function representing the detector element and $\mathfrak{R}_{\text{diff}}(\lambda, x)$ is the line spread function response of the optics including diffraction. In this manuscript we describe wavelengths and distances in spectral and spatial units of microns, μm. For clarity, spectral units, for example, λ are given the symbolic abbreviation (μm) and distances, for example, the slit width, l_{sw} units are written out as microns.

The large bandwidth of TIRS, and designed diffraction limited performance beyond 30 μm, necessitates the instrument function be explicitly calculated at several sub-pixel (wavelength) steps, and then convoluted with both the detector and slit sizes. The width of the function, γ for a given wavelength defines the spread function $\mathfrak{R}_{diff}(x)$ over the spectral dimension of the pixel. The spectral resolution is then the FWHM of the spectral response function where $\Delta\lambda_n$ = Spectral resolution of the nth detector element (μm)

$$\mathfrak{R}_{\text{diff}}(x) = \left[\frac{\gamma \sin(\pi x/\gamma)}{\pi x}\right]^2, \Delta\lambda_n = \text{FWHM}(\mathfrak{R}_{n,\lambda}) \tag{4}$$

The TIRS presented here has $\Delta\lambda_n = 1.71$ μm below 35 μm sampled at 0.86 μm increments. Although diffraction spreads out the longer wavelengths at the focal plane into adjoining pixels, this may be thought of as a blurring of the adjacent along-track scenes and not a loss of signal. The convolution with the slit and detector widths properly accounts for this effect as long as the adjacent scenes are spectrally similar. Caveats for geometric calibrations apply.

The spectral channels are modulated by $\mathfrak{R}_{n,\lambda}$, and attenuated by the grating efficiency $\rho_{g,\lambda}$ as well as the order sorting filter transmission $\tau_{f,\lambda}$. The channels detect the spectral radiance, $I_{\text{total},\lambda}$, projected onto them from all angles, only light passed through the slit is spectrally modulated and the spectral response function for a given spectral channel, n, or $\text{SRF}_{sc,n}$ can be defined as

$$\text{SRF}_{sc,n}(\lambda_i) = \rho_{g,\lambda_i}\tau_{f,\lambda_i}\mathfrak{R}_{n,\lambda_i} \tag{5}$$

where λ_i is discretized onto a grid (1 to N, where $N \gg n$) that is significantly finer than the channel width to minimize errors due to filter, grating and diffraction spectral dependences.

The total irradiance sensed, $I_{\text{total},n}$ is a combination of external and internal irradiances in which the irradiance from the external scene, $I_{sc,n}$, the spectral dependent emission of the optics, attenuated by filter transmission $I_{\text{sc}',n}$, the emission of the filters themselves, $I_{\text{em},n}$, and the emission of the detectors, $I_{\text{det},n}$ are measured as a voltage difference from the effective temperature of the focal plane, with effective power estimated by T_D, as given by the Stefan-Boltzmann law,

$$I_{\text{total},n} = I_{sc,n} + I_{\text{sc}',n} + I_{\text{em},n} + I_{\text{det},n} - \sigma T_D^4 \tag{6}$$

For a more thorough description of the theoretical basis of TIRS imagery, the PREFIRE Level 1 algorithm theoretical basis document is available at the (“Atmospheric Science Data Center”, n.d.) along with the Level 1 data. During nominal operations, the summary contributions of the background signals $I_{\mathrm{sc}\prime,n}$, $I_{\mathrm{em},n}$, $I_{\mathrm{det},n}$,and T_{D} are determined through active calibration sequences in which the instrument is commanded to observe an internal uniform scene of temperature, T_C, as well as an external view of cold space at temperature, T_S.

The real signal, or sensible voltage, V, is a signal from the combined Field-of-View (FOV) and instrument itself. For a given detector in a given integration time V is given by

$$V_{sc,n} = l_p^2 \wp_{sc,n} I_{\mathrm{total},n} \tag{7}$$

where $\wp_{sc,n}$ is the pixel specific detector responsivity, and l_p^2 is the detector area. We use $\mathbb{S}_{sc,n}$ to describe the digitized voltage signals that incorporate instrument electronic gain settings. We describe the contributions to the irradiances, I, measurements ${}^{meas}\mathbb{S}$ (meas $= C$, S for each calibration scene, $\mathbb{S}$ are digitized voltages). For calibration and conversion from counts to scientific units, ${}^{C}I$ and ${}^{S}I$ are approximated as blackbodies and isolation of the external scenery allows for introduction of well-defined scene and wavelength specific spectral radiances, ${}^{C}L_{sc,\,n}$ and ${}^{S}L_{sc,\,n}$. In this way the calibration measurement quantifies the unknown instrument background signals and establishes the a priori unknown gain associated with conversion of voltage to scene spectral radiance. Crucially, the instrument thermal signals in science imagery must be interpolated between calibration scenes with low error. The two point calibration measurements and known target spectral radiances directly determine the variable, $g_{sc,n}$, known as radiometric gain. Interpolation and application of the gain provide the desired final radiometric quantity of the Earth scene spectral radiance $L_{sc,n}$. The gains can be expressed as:

$$g_{sc,n} = \frac{{}^{C}\mathbb{S}_{sc,\,n} - {}^{S}\mathbb{S}^{sc,\,n}}{{}^{C}L_{sc,\,n} - {}^{S}L_{sc,\,n}} \tag{8}$$

where the ${}^{C}L_{sc,\,n}$ and ${}^{S}L_{sc,\,n}$ are the spectral radiance of the internal calibration target and the space view, convolved with the instrument SRF at scene sc and spectral channel n. This ratio $g_{sc,n}$ converts the detector counts ($\mathbb{S}$) directly into spectral radiance L. The SRF convolution of an arbitrary spectral radiance $L(\lambda)$ into measured radiance at scene sc and channel n is performed in the standard way:

$$L_{sc,n} = \frac{\int_{\lambda_n}^{\lambda_{n+1}} L(\lambda)\ \mathrm{SRF}_{sc,n}(\lambda)\ d\lambda}{\int_{\lambda_n}^{\lambda_{n+1}} \mathrm{SRF}_{sc,n}(\lambda)\ d\lambda} \tag{9}$$

Application of the gain to the measured earth signal allows calculation of the calibrated Earth view spectral radiances, $L_{sc,n}$:

$$L_{sc,n} = \frac{\mathbb{S}_{sc,n} - {}^{S}\mathbb{S}_{sc,n}}{g_{sc,n}} \tag{10}$$

3. Implemented Design

To accomplish PREFIRE science, we fly two spacecraft each with a Thermal InfraRed Spectrometer (TIRS), such that each can each make over 200 million spatially and spectrally resolved observations of Earth's polar radiant thermal energy in a year. These spacecraft must conform to CubeSat launch standards to enable low-cost access to space. Therefore we adhered not only to strict spaceflight hardware protocols, but also volume (<4U, 1U = 1L), power (<6.2 W) and mass (<3.5 kg) restrictions for accommodation on a 6U bus (see Table 1). Initial design efforts are briefly described in Padmanabhan et al. (2019), here we detail the as-built system.

3.1. Characteristics, Requirements, Accommodation

High performance thermal-IR systems (Fisher et al., 2020; Hulley et al., 2016) with cryogenic detectors have enabled fine-spatial sampling only at (technology limited) wavelengths shorter than 16 μm. High performance technologies (Wielicki et al., 2013; Zmuidzinas, 2012) beyond 16 μm require large volume, mass and power for cryogenics and, for Earth observing, also require high resolution spectrometry to split the energy of the spectrum into small pieces that do not overload the ultra-cold sensors. Conversely, filter radiometers, such as the Mars

Table 1
TIRS Science Requirements, Design and Performance Characteristics

			Performance	
Property unit	Specification	Design[a]	TIRS1	TIRS2
Mass	3.5 kg	3.1 kg	2.7 kg	2.7 kg
Volume	4.0 U	3.2 U	2.74 U	2.74 U
Power	6.2 W	5.2 W	4.3 W	4.3 W
Data rate	16.0 kbps	12.9 kbps	12.9 kbps	12.9 kbps
Spatial Sampling	1.5°	1.3°	1.3°	1.3°
Spectral Sampling	1 μm	0.86 μm	0.86 μm	0.86 μm
Spectral Bandwidth	5-35 μm	4-54 μm	6- 36 μm	6- 36 μm
NEDT_{300} < 15μm	1.6 K	0.8 K	<2.1 K	<0.8 K
NEDT_{300} 15–25μm	2.8 K	1.4 K	<1.4 K	<1.4 K
Thermal Control	±1.5 K	±0.5 K		

[a] Design values are those estimated at Critical Design Review.

Climate Sounder (MCS (McCleese et al., 2007)) and Diviner Lunar Radiometer Experiment (DLRE(Paige et al., 2010)) enable ambient thermal imaging (at any wavelength), but are not readily miniaturized. Furthermore, filter widths limit radiometric bandwidths to greater than 5 μm in channels beyond 19 μm (Blanchet et al., 2011), limiting science in the so-called "dirty" window important to Arctic energy exchange (Peterson et al., 2019; Xie et al., 2023).

To retrieve the required quantities of spectrally resolved thermal imaging data, an instrument trade study for a small satellite mission was performed. Recognizing the limitations just discussed, science goals originally consistent with the CLARREO concept (Wielicki et al., 2013) were revisited with a focus on how much spectral information content was required to radiometrically characterize thermal emissions in polar regions and to determine at what spatial and temporal scales melt processes and atmosphere/cloud interactions would manifest. Several results of the trade study are notable here: (a) To keep mass, power and costs low, an uncooled focal plane was deemed essential; (b) for even sampling of cloudy and clear scenes in the polar regions ground sampling distances of roughly 20 km are desired; (c) roughly 10 unique spectral regions need to be sampled to separate confounding factors in the radiative balance across the Earth's thermal emission. These results led us to hone a concept for broadband thermal spectral imaging.

To achieve <1 μm sampling, we have adopted the ambient temperature focal planes of MCS/DLRE (McCleese et al., 2007; Paige et al., 2010), coupled with the Offner design of the Moon Minerology Mapper (M^3) instrument (Green et al., 2011; Van Gorp et al., 2014). This technical implementation of thermopiles in an imaging spectrometer is theoretically equivalent to an imaging radiometer with narrower, overlapping filters. Although not a filter radiometer, filters are still important in TIRS design. Instead of defining science channels as in MCS/DLRE, the filters in an imaging spectrometer serve to block undesired wavelengths from higher order diffraction that necessarily overlap the primary diffraction order in a broadband (multi-octave) wavelength range. The filters are thus called order sorting filters. This usage loosens technical requirements on the filters while allowing the diffractive optics to enable a high efficiency, compact architecture. This also provides science with a wide bandwidth and multiple separable radiometric degrees of freedom (Xie et al., 2022). Based on existing technologies (block diagram in Figure 1) two compact, all reflective diffraction Thermal InfraRed Spectrometers (TIRS) have been built. Each TIRS consists of an (a) Detector Array and Read Out Integrated Circuits (Section 3.2); (b) Order Sorting Filters (Section 3.3); (c) Schwarzchild Telescope and Offner Spectrometer (Section 3.4); (d) shaped-grooved grating (Section 3.5); (e) Pointing Mirror Calibration System (Section 3.6) (f) Thermal subsystem (Section 3.7); and (g) Instrument Control Electronics and Software (Section 3.8).

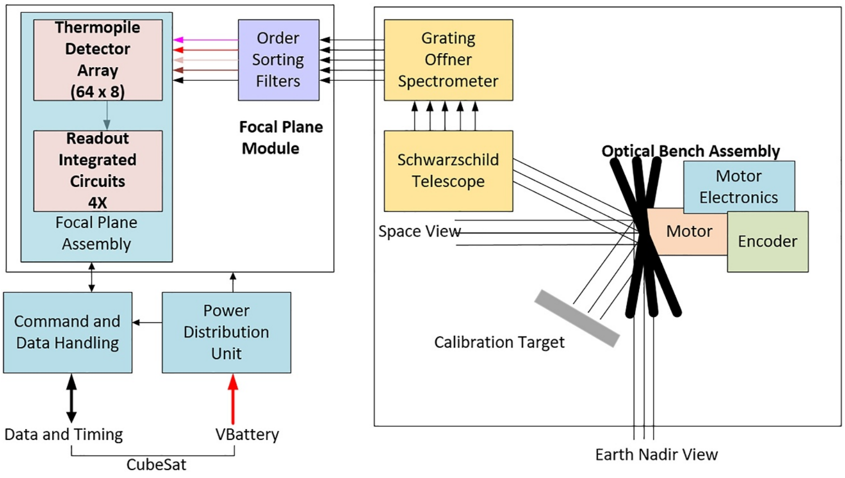

Figure 1. Block diagram of the TIRS instrument.

By design each TIRS makes pushbroom imaged spectral maps from polar orbit with 54 unique spectral channels covering eight non-contiguous cross-track spatial scenes at 0.86 μm sampling with images recorded continuously every 0.707 s. Crucially, each TIRS is thermally regulated with a thermal sub-system, and science images are captured on a high duty cycle, with at least eight periodic views of space and internal calibration target during each orbit. Both the nadir view and the space view are un-obstructed free-space paths through the instrument optics, as selected by the pointing mirror. The combination of an Offner diffraction spectrometer (Prieto-Blanco et al., 2006) with ambient thermal imaging (McCleese et al., 2007; Paige et al., 2010) is a novel implementation of compact, low mass, low power technologies developed for filter radiometry and optical imaging that meet the PREFIRE requirements of measuring the Earth's longwave radiation from orbit as shown in Table 1.

The CubeSat supplies command control via the CubeSat S-band uplink, and this control is verifiable through housekeeping data provided. The CubeSat also provides an S-band transmitter for science data downlink and other housekeeping data. Instrument power is provided from the CubeSat power system. The CubeSat avionics provide pointing control and knowledge. As shown in Table 1, as built TIRS units consume 4.3 W power that must be supplied from the spacecraft power subsystem.

3.2. Detector Array and Read Out Integrated Circuits

The detector (see Figure 2) is a 64 × 8 pixel arrangement of individually wired thermopile sensors. Each detector pixel is $l_p^2 = 0.18\ \text{mm} \times 0.18\ \text{mm}$. The 64 contiguous pixels form the spectral, or x, dimension of the imaged spots and also project into the along-track field at 3.3°. The eight separated pixel strips that span the y dimension each image a 1.3° wide spatial location in the horizontal direction of the imaged scene. Optical properties of the system will be decribed in a later section, through regular capture of thermal imagery during flight, three-dimensional thermal imagery of the nadir scenes are constructed.

TIRS uses thermopile detector technology (Mariani et al., 2019; Mariani & Kenyon, 2015) developed at JPLs Micro Devices Laboratory (MDL). This detector technology has been flying on MCS for over 15 years to study the Martian climate and was flown on DLRE for 8 years to study the thermophysical properties of the Moon's surface. For TIRS, the format size of the arrays has been chosen from a format developed for planetary science that meets both sensitivity and spatial sampling requirements for PREFIRE.

Thermopile sensors quantify scene radiance through absorption of incoming radiation in a convectionless environment, such that an ideal detector has emissivity of unity. The process of coating the detector array with gold black resist, which provides optimal performance, has been engineered for these large format detectors to enable: (a) specific coating thicknesses, with 30 μm depth determined appropriate for the TIRS bandwidth; and (b) targeted laser trimming to isolate pixel responses. This capability to trim gold-black with incident radiation also highlights the potential for inadvertent gold-black ablation from direct, instrument focused, sun exposure. Calculations suggest short exposures to direct solar radiation could significantly degrade sensitivity, a situation that drives certain TIRS and spacecraft requirements. The process was developed with system level (focal plane, ROICs and cabling) testing that demonstrated optimal detector performance, before being applied to the two flight units.

Detectors with a return yield of 90% or higher pixels for spectral channels covering a majority of the Earth's Planck emittance, and an unfiltered noise figure of <0.25 K NEDT at the 300 K blackbody peak were accepted for integration into flight units.

TIRS uses flight-qualified Read-out Integrated Circuits (ROICs) from Black Forest Engineering. Unlike MCS and DLRE, these next generation ROICs have integrated analog-to-digital converters that enable simplification of connections and associated instrument electronics. Their performance is detailed in the Supporting Information S1 and Figure 2 (left) shows the board where the four ROICs are co-mounted in a square around the active detection region. Wire bond connections are made for each pixel (1024 wires) to the parallel ROIC inputs, and ROIC outputs are multiplexed for transfer to the electronics subsystem through a miniature connector and cabling. Additional wiring for clock, power and SPI communications are included in the same connector. The wires are bundled and shielded to avoid signal loss and noise pickup.

There are two noise sources that dominate the thermopile/ROIC subsystem. These are Johnson noise of the thermopile and ROIC read noise, the noises are characterized in tandem and depend on the thermopile resistance,

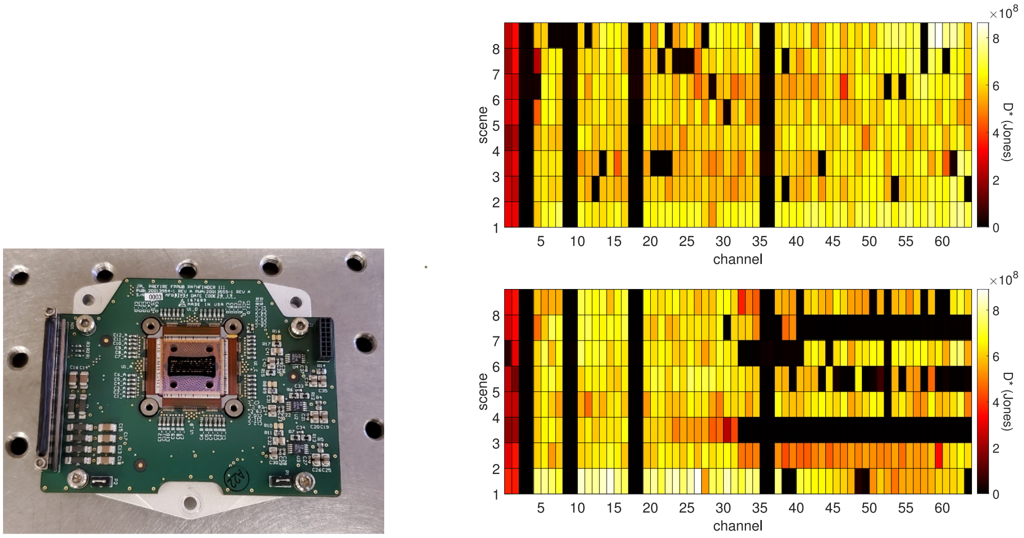

Figure 2. (left) Photograph showing thermopile detector and ROICs mounted on printed circuit board, breadboard in background is 1″ lattice for scale. (right) Pixel maps showing measured responsivity (Jones = W^{-1} cm $Hz^{1/2}$), TIRS1 upper, TIRS2 lower.

R_d, and the ROIC integration time, t. Thermal noise of the detector is added in quadrature with associated ROIC amplifier noise, and both are spectrally flat. The thermal noise contribution to the power is $\sqrt{kT_{\text{det}}R_d/t}$. Additional noise is detectable at longer integration periods, with ROICs test systems showing a common-mode noise build up due to additive capacitances along each ROIC sub-unit (64 channels). To minimize this effect, each consecutive channel was wired with opposing polarity to neighboring channels. Alternating polarities in a flat field image then add up to zero total capacitance and the common-mode noise dissipates. Since consecutive pixels in the full system measure different radiances across spectral scenes, there are small biases (below the SNR of single images), that is, "cross-talk" remaining in the sensible voltages. Noise associated with gain stability is characterized on orbit and minimized through optimization of the calibration cadence. The effect at the system level is described in the supplement and a basic model is under development.

3.3. Order Sorting Filters

The grating diffracts 30%–40% of the incident radiation along the first-order ray paths. Roughly 20% of the light is directly reflected onto the first, unfiltered, row of the focal plane (zeroth order). The remaining 40%–50% of the incident radiation is projected along higher-order paths that would produce confounding signals in the wideband thermopile pixels. An array of order-sorting filters covering four consecutive octaves minimizes detection of this stray light.

The first three orders, from 5 to 30 μm, are interference filters. The InfraRed Multilayer Laboratory (IML) specializes in the manufacture of these interference filters and Oxford Space Instruments Laboratory (SIL) had previously provided filter blocks with IML filters for the MCS and DLRE instruments. The filter specifications were derived from the designed spectrometer bandwidth are given in Table 2. The IML provided multi-layer coated substrates of Zinc Sulfide, Zinc Selenide and Cadmium Telluride for the selected bandpasses of filters #1-#3, respectively, filter #0 was chosen to be uncoated diamond. Filter thicknesses were varied in accordance with substrate refractive indices to keep the depth of focus homogenous. Designed bandpasses utilizing the multilayering techniques have sharp edges and characteristic ripples in the bandpasses associated with the multiple etalons created in the multi-layers. To reduce harmonically related sidebands (undesired passbands at multiples of the desired passband) the Zinc Sulfide filter (#1) was combined with a MgF_2 section that provides blocking of all longer wavelengths (Seeley et al., 1979).especially the 12–15 μm light that is abundant in earth's thermal envelope.

For filter #4, consideration for coated diamond substrates were rejected due to bandwidth limitations. Therefore the 30–54 μm range required a mesh filter. Stock of an appropriate mesh filter was available at SIL and

Table 2
Band-Pass Filter Definitions (in μm)

Band	λ_1	λ_2	λ_3	λ_4	λ_5	λ_6
#0	-	-	-	-	-	-
#1	≤ 0.5	3.65	3.86	7.29	7.72	>16.0
#2	≤ 2.0	7.07	8.14	14.14	14.6	>29.8
#3	≤ 3.6	14.78	15.0	29.57	30.0	>59.2
#4	≤ 7.4	28.6	30.43	-	-	-

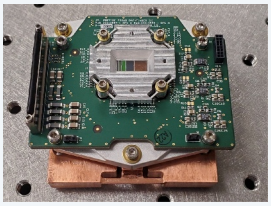

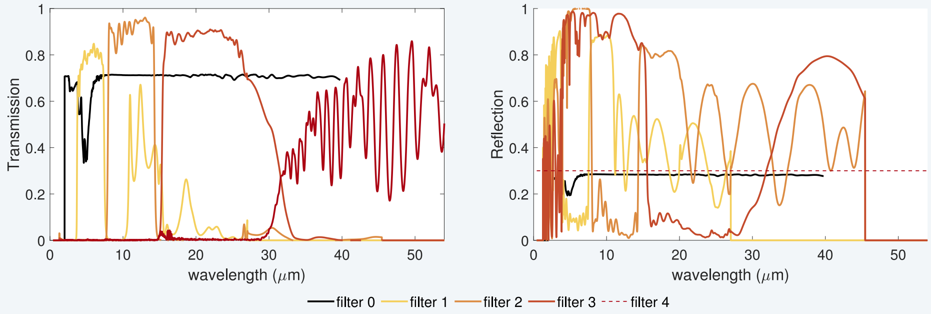

Note. (λ_1 to λ_2) and (λ_5 to λ_6) are the blocking regions ($\tau_f < 1 \times 10^{-3}$ desired). λ_3 and λ_4 are chosen to fall on the edges of each filter spectral rangeThe gaps between blocking and transparent regions (λ_2 to λ_3) and (λ_4 to λ_5) are unimportant spectrally and are meant to be wide enough for the transitions of the filter spectral responses. Filter #1 is shown without MgF_2 blocking.

development efforts focused on creating a uniform (flat) surface with matching refractive properties to the other filters. The chosen implementation solves both of these concerns simultaneously, albeit with a notable consequence of significant fringing. The mesh grids for each flight unit were placed between two pieces of diamond, all pre-cut to appropriate dimensions for gluing and clamping into the filter assembly. The total diamond thickness matches the refraction to other filters, however, the internal reflections between the diamond surfaces, separated by the 50 μm thickness of the mesh, create an oscillatory structure (see graphs in Table 2 and Supporting Information S1) on the order of the TIRS spectral sampling.

In the FIR, it is not unusual for ripples of varying depths to undulate through the bandpass range. TIRS filters are not required to be flat and spectral characteristics are determined with component testing. As built filters #1-#3 achieve 70%–90% transmission, with adequate blocking to achieve the order-sorting. Science requirements regarding the capture of *most* of the Earth's thermal envelope allowed for the acceptance of the ~50% transmission of filter #4.

Filters were characterized at SIL using a Perkin Elmer Spectrum 2000 Optica FTIR (1.5–40 μm) spectrophotometer and a Hitachi U3400 UV-VIS-NIR grating spectrometer (190–2,600 nm) to determine transmission $\left(\tau_{f,\lambda_i}\right)$ for instrument modeling. For MIR/FIR accuracy the Spectrum 2000 was modified to reduce inter-reflections and non-linearities in the electronics were compensated. A beam size of 7.0 mm uniformly illuminated an $f/8$ cone and repeated background measurements assured reproducible results. Collected data are available in Supporting Information S1 and used in the instrument model, Figures embedded in Table 2 show the transmission and reflectance measurements graphically.

The filters were assembled into a unit and environmentally tested prior to delivery for instrument integration. The assembly is large enough to have significant heat capacity for the filters to equilibrate with the instrument. The recessed filter tray holds the filters within 100 μm of the focal plane surface (not including the gold-black deposited to 30 μm depth). Strips between filters were made as narrow as possible to minimize the number (2) of "sacrificial"

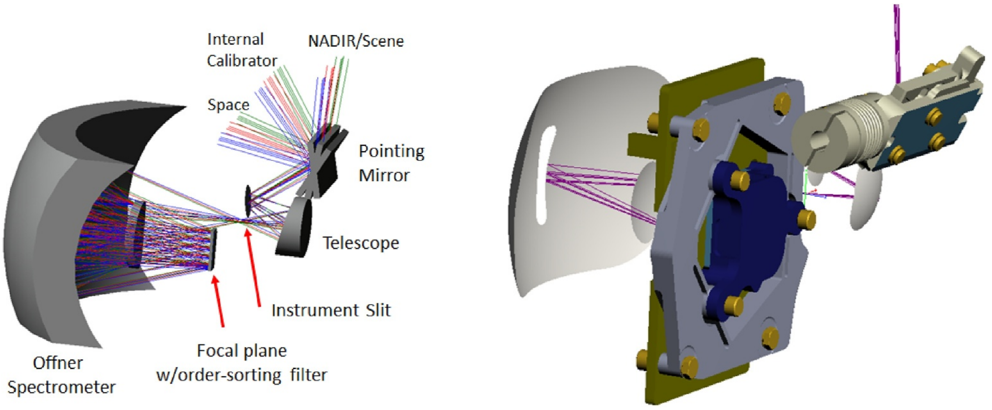

Figure 3. (left) Optical design of TIRS showing pointing mirror in three possible looks nadir/science (N), internal calibrator (C) and cold space (S). Ray paths then trace out through the telescope, slit/focus location, Offner spectrometer with grating on curved inner surface, and finally, termination at focal plane. (right) partial computer design view including detector (shown from backside) and pointing mirror assembly. Rays shown are those intended to be scattered by the tailored cutout (white region in center of toroid surface), notice these rays straddle the grating.

pixels that are blocked or partially blocked underneath these zones. The photograph embedded in Table 2 shows the filter assembled onto the focal plane, the image shows the filters ordered #0-#4 from left to right.

3.4. Schwarzschild Telescope and Offner Spectrometer

The Offner architecture shown in Figure 3 provides linear dispersion at the focal plane in the 5–54 μm range. The instrument Instantaneous Field of View (IFOV) is injected into the slit with a Schwarzschild Telescope, after the slit a custom grating and mirror form the inner and outer surfaces of a toroid, respectively. Figure 3 shows a ray trace through these optics; rays for both spatial (parallel lines of same color) and spectral (blue or red) paths are shown. The dimensions for this design conform to the 6U cubesat form factor, with the toroidal mirror (longest dimension) at 85 mm. For maximal radiometric illumination from the instrument field-of-view, optical design minimized f in both spatial and spectral dimensions. The final design is anamorphic, with $f = 1.8$ in spatial (cross-track) and $f = 1.6$ in spectral (along-track) dimensions. The telescope design provides an 8.0 mm focal length in the cross-track dimension, f_l, to achieve $\alpha = 1.3°$ cross-track spatial resolution ($\alpha = l_p/f_l$), and the focal length in the along-track/spectral dimension is 6.5 mm. Due to the use of a slit with dimensions 0.36×4.00 mm, or $2l_p$ wide, the along-track instantaneous field of view is thus 3.3°, a design choice that reduces spectral resolution but maximizes radiometric signals without compromising information content for scientific return.

Modeling of the optical design provides an overall instrument (including grating and filters) efficiency of 20%–27%. The analysis shows no significant keystone effects on the IFOV and a <6% divergence of horizontally aligned pixels in the spatial view. The unconventional placement of the zero order (reflection) of the grating onto the active sensor introduced the possibility for irradiance from outside the nominal IFOV (i.e., when nadir view is flooded with illumination) that skips the grating and reaches the detector in a single bounce off the central portion of the toroid mirror. This section of the toroid mirror is not used for nominal light paths, but is typically present as a contiguous portion of the free-form toroidal surface shape that is used for capturing the incoming light and redirecting the diffracted light on either side. The single bounce path was quantified in calculations that provided the distribution of irradiance and total flux on the detector following the unintended path, relative to the light which follows the design path. The effect was found to be significant, with up to 9% of the zero order signal sourced from out of the intended field. Mitigation was made in the form of a tailored cutout in the center of the mirror, with the resulting hole forming a blackened well which reduced the calculated effect on the zero order signal to ~0.3%.

Two complete optical bench assemblies were delivered by optics developer II-VI, alignment metrics included some ambiguity about precise placement of the focal plane in the spectral dimension.

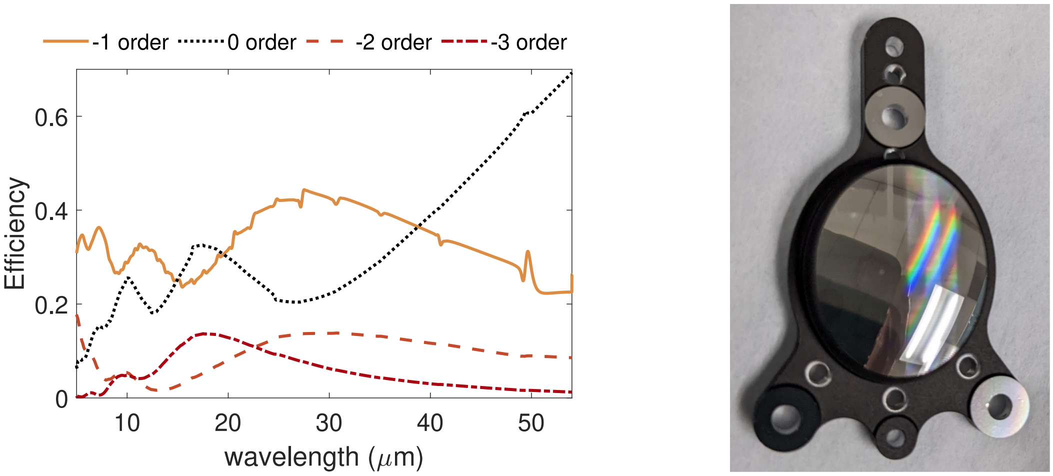

Figure 4. (left) Grating efficiency based on shaped groove modeling, wavelength dependent diffraction efficiencies, ρ_{g,λ_i}, where g is the order, are used in the instrument model. (right) Image of shaped-groove grating.

3.5. Shaped Grooved Grating

TIRS utilizes an aluminum, machine cut, shaped (3 segments) grooved surface (Mouroulis et al., 1998, 2003) for high efficiency, 5–54 μm bandwidth dispersion of thermal energy evenly along the focal plane at 0.86 μm sampling on the detectors. For scientific interest, the undispersed (reflective) broadband thermal energy, or 0^{th} order, of the grating, is also passed onto the detecting area.

The grating design achieves 25%–40% efficiency (ρ_{1,λ_i}, see Figure 4) in first order across the band, peaking in the 20–30 μm range of primary interest to the PREFIRE science objectives.

In addition to capturing the pure reflection (0th order) and primary (1st order) of the grating, other (higher) grating orders propagate onto the detector plane and produce signals if not absorbed or scattered by the filters. The wavelengths, at a given channel, of this undesired radiation are related through the linearized grating equation. Orders other than the 1st order fall outside of the designed filter bandwidths, such that the minimal filter transmission τ_{f,λ_i} at these positions attenuates the light.

3.6. Pointing Mirror Calibration System

The TIRS instrument utilizes a mechanically tuned flat mirror to orient the telescope objective onto either of two calibration positions (C,S) or the position for science (N) (see Figure 3). Due to risks associated with exposure of the focal plane to focused solar radiation, a failsafe system is also implemented as part of this assembly. Details of the parts in this system are given in Supporting Information S1.

The motor has a maximum of 54 N·mm torque to position the mirror reproducibly against a constant force (22 N·mm) spring. The springs are poised within a custom bracket to pull the mirror to the fixed hard stop when no power is provided to the motor. The fixed hard stop position provides negligible optical exposure for the focal plane to external radiation. During normal operation the mirror actuator is energized to work against the torque of the failsafe spring.

The motor operating positions are determined from functional testing using feedback from the encoder and the instrument radiometry so that calibration sequences can be executed periodically by micro-stepping the actuator between positions. The instrument is designed for nadir staring, interrupted by occasional slews of the pointing mirror where it spends several image frames (0.707 s) collecting calibration data at both calibration positions. The nominal sequence is HSCN[SCN]X where S,C,N were defined in Figure 3, and H is the hard stop where the instrument rests until energized, square brackets indicate a repetitive loop, and X is either C if the instrument is placed in safe mode, or H if the instrument is de-energized. Staring times at each position are configurable, slew times are less than one image frame for NC transition and between 1 and 2 frames for NS and SC transitions.

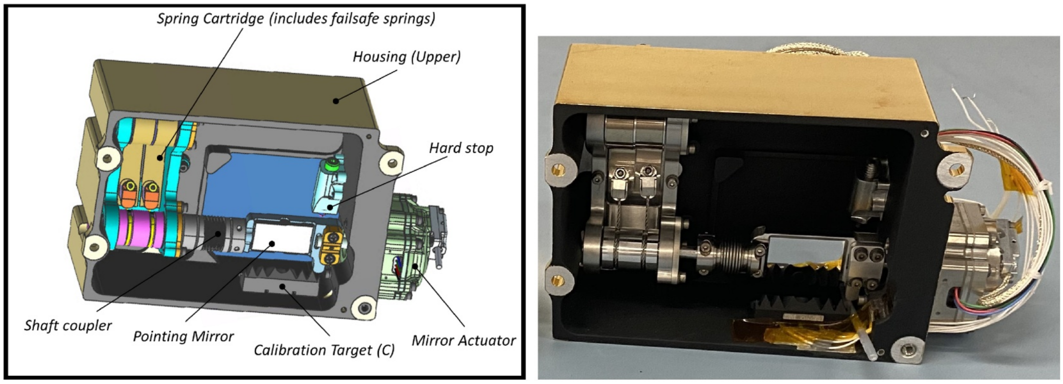

Figure 5. (left) Diagram depicting the pointing mirror assembly. (right) photograph of assembled hardware.

Figure 5 shows the design, as well as a photograph, of the pointing mirror calibration system. An open aperture located over the toroidal mirror allows for observation of cold-space at position S for nominal nadir pointing in low earth orbit. Within the instrument housing a custom calibration target can be viewed at position C. This target is a grooved aluminum surface painted with Z306 paint and fitted with three thermistor sensors that monitor the temperature. Grooves are in a radial pattern that redirects rays projected from inside TIRS onto neighboring grooves, multiple ray bounces off the high emissivity surfaces, by design, ensure that TIRS views of thermal energy in this pointing position originate from the known temperature target. Conversely, reflected light from inside the housing or from either aperture is strongly attenuated through absorption onto the target. Like the calibration target, much of the insides of the TIRS are also painted with high emissivity Z306 paint, this minimizes potential for stray light leakage into the imagery.

3.7. Thermal Subsystem

TIRS incorporates a passively regulated thermal design. Figure 6 provides a simple thermal architecture overview and photograph depicting the thermal strap. Heat generated by the scan motor and encoder is conducted to the instrument enclosure. Heat generated by the focal plane assembly is conducted through the optics bench. A thermal strap is used to dissipate heat from the focal plane electronics to the optics bench to reduce thermal gradients between the optics and focal plane. Heat generated by the instrument electronics is conducted directly to the spacecraft. The optics housing is attached to the spacecraft bus via thermal isolators. Thermal modeling of the system shows that 3.5 K variations in spacecraft temperature over on orbit result in 1.5 to 0.5 K variations of the focal plane and calibration targets, respectively. Thermistor measurements throughout the TIRS system and calibration sequences that subsample this thermal variation then enable modeling of the thermal environment within the instrument on a continuous basis as necessary for background signal removal from imagery. A more detailed analysis is available in McKinley et al. (2022).

3.8. Instrument Control Electronics and Software

A Power Distribution Unit (PDU) converts and isolates the spacecraft power for the TIRS instrument, serving as the only interface to the spacecraft systems, it passes through communications to the TIRS command and data handling (CDH) unit, details of the components are given in Supporting Information S1.

The command control functionality allows the instrument to operate in three modes: (a) science, (b) safe, and (c) test. Science mode operates the regular duty cycle of the pointing mirror assembly, each frame encompassing all of the pixel signals summed over 0.707 s. Calibrations are performed after a set number (configurable on orbit) nadir frames, with partial images formed while the motor position changes followed by a clear image at rest on each alternate rest position (N,S,C). In safe mode, the motor position is moved to the internal calibration target and fixed until removed from safe mode. Test mode (for ground measurements or special flight operations) enables specific motor positioning.

One hundred twenty-eight detector pixels are multiplexed in each ROIC, and the ROIC signals are delivered from the FPA/ROIC assembly via a custom cabling harness (visible in Figure 6). In addition to packetizing TIRS

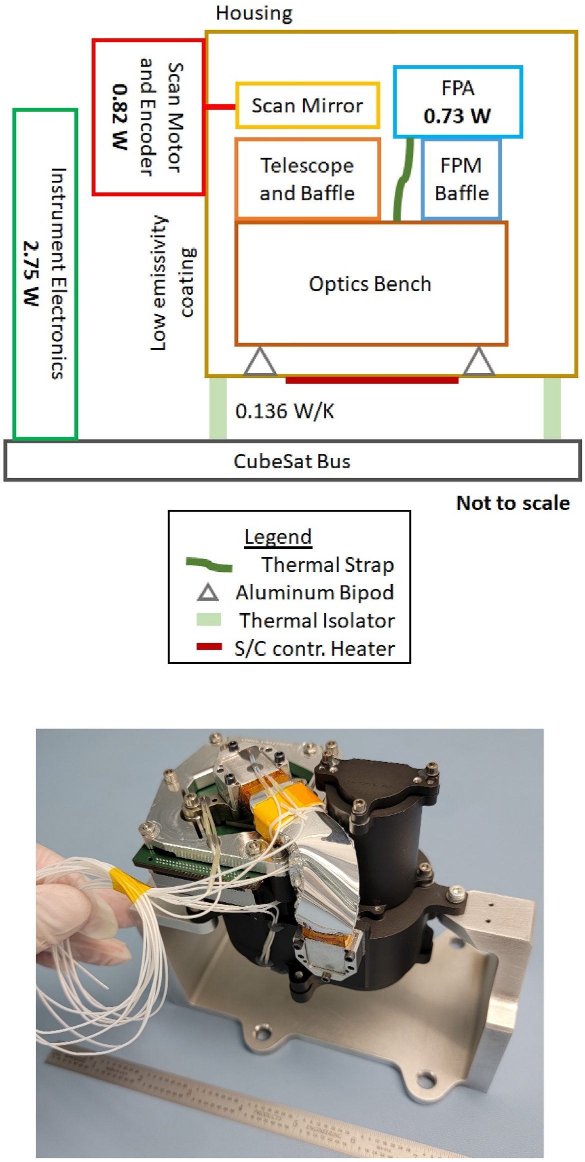

Figure 6. (upper) Thermal architecture for TIRS showing active and passive components and thermal connectivity. (lower) Photograph showing thermal strap (bright metal) connecting FPA (oblique surface in upper left) and Optics Bench (black), also visible are the telescope and baffle (black, upper right) and thermistor cables (white wires).

imagery (1024 bytes), 80 bytes of engineering data is embedded in each header, comprising: 8 thermistor readings, 4 ROIC temperatures, 4 thermocouples, 6 voltages, 13 current readings, and the present encoder value (there are 4 unused 2 byte registers). An additional 19 bytes of synchronization markers, packet identifiers, counters, timestamps and checksums fill out the 1142 byte science packet. Thus the nominal TIRS data rate is set by the combination of these digitized signals every 0.707s to be 12.9 kbps.

System power consumption is given in Table 1, as shown in Figure 6 the ROICS consume 0.824 W, the motor board consumes 0.73 W and the rest of the electronics are 2.75 W. The data buffer can hold multiple days of continuous raw data. The spacecraft flight software periodically polls the instrument to push out these data blocks for storage, prioritization and later transmission.

4. Instrument Testing and Calibration Results

The instrument testing program includes a complete verification of key specifications including sensitivity, field size of each pixel, and frequency response, all measured in thermal vacuum chambers (TVC). Schematics of the setup are available in the Supporting Information S1. Both TIRS instruments, referred to here separately as TIRS1 and TIRS2, were operated through a Blue-Canyon Technologies (BCT) spacecraft simulator (FlatSat) that simulates the spacecraft bus electronically. A summary of instrument testing is given in Supporting Information S1, details are given in the upcoming subsections.

4.1. Functional Testing

Benchtop aliveness tests establish basic systems responsiveness and nominal telemetry. These tests were performed at initial assembly prior to application of epoxy to connectors as well as after vibration testing. The TIRS1 instrument passed all benchtop aliveness tests. In initial post-assembly benchtop aliveness testing, the TIRS2 instrument was shown to have a disconnected pin, the issue was then fixed at the appropriate wire-harness end point and verified with a repeated test. With the exception of benchtop and vibration testing, all further instrument testing activity is performed in a TVC to mitigate the effects of water vapor absorption and to allow the detectors to operate in a convection-free environment.

Further functional testing of each instrument involved stepping the motor through its full range of motion (scanned at four encoder positions per step) while hot (310 K) and cold targets (120 K) were presented to the nadir/science and space/calibration views, respectively. Aperture locations and associated encoder values were found to be consistent with the design. No discernible thermal features are observed in the vicinity of the internal calibration target, implying that the target and the region around the calibration target are isothermal. The final functional test was designed to discern if basic radiometric response times were adequate for proceeding with further testing. This test can be described as a sequence HSCNSCNSCNSCNSCN in which each SC segment has a progressively longer dwell times at S and at C. Dwell times of 3, 4, 8, 16, and 32 s were chosen. Channels under filters 0,1,2,3 all exhibited “square” responses, that is, showing no lag effects during time periods on the differing temperature targets. However, in channels associated with filter 4, an increasing lag is observable with increasing wavelength. Short exposure times minimize the temperature change and provide reproducible gains without further correction up to 36 μm, beyond this range, a time dependent calibration that accounts for the calibration induced perturbation and return to steady-state will need to be developed.

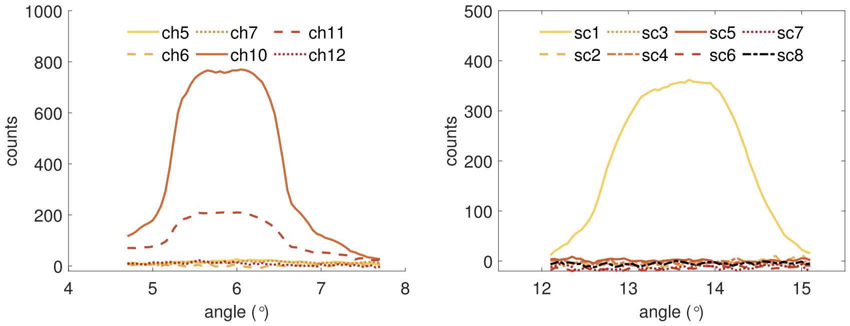

Figure 7. (left) Example, background subtracted, azimuth scan over TIRS1 scene 3 with 8.44 μm illumination showing adjacent spectral pixels. (right) Example, background subtracted, azimuth scan over TIRS2 scene 1 with 8.44 μm illumination showing all scenery at $n = 10$.

4.2. Optical Alignment—Spatial Calibration

Spatial calibration pre-flight measurements were made to support algorithm geolocation through determination of cross-track and along-track instantaneous field-of-view for broadband and shortwave pixels, and to support implementation of the geometric instrument model for relative alignment of all pixels. Two types of tests were designed to evaluate the instantaneous field-of-view for each of the TIRS instruments, for which imperfections in components or misalignments in assembly could potentially produce non-uniform fields and/or induce spectral dependencies of the ground footprints. These tests, in combination with spectral characterization (described in next section) provide a comprehensive evaluation of the critical factors in developing an instrument model of each TIRS imaging spectrometric capability.

From an optical perspective, the ground track distance is a projection of the focal length, such that determination of the angular edges of the fields of view at well known wavelengths are sufficient to parameterize the instrument model and subsequently project the IFOV into geocentric coordinates from orbit. For generation of collimated radiation for optical testing, two co-aligned light sources were developed and characterized extensively. The exit collimation was 4 mm, corresponding to one pixel width at the instrument entrance aperture. For expediency, no absolute alignment was attempted between the light source and the instrumentation under test. Systematic 1D scanning of the azimuth and elevation through nominal pixel centers at each field point was conducted, with initial scans designed to refine the origin through iterative azimuth sampling as determined in real-time analysis. These scans were repeated at each field point and at available laser wavelengths representing nominal pixel center and edge wavelengths, as shown in Figure 7.

Inspection of Figure 8 as well as analysis of the full-widths of the fields, show that each field of TIRS1 has flat angular dependence and demonstrate no clocking (*xy* or cross-track spatial/spectral) errors as well as no significant misplacement of the physical pixels into the optical focal plane. All data is consistent with designed full-width fields of 1.3°. An observed ∼1% deviation (0.25° at extremes of 28° swath) of the centroids, versus the nominal design, is attributed to a real focal length difference (from design) of 1%. The measured focal lengths (and other nominal instrument geometric parameters) are used in the instrument algorithm in the projection of the instantaneous field-of-view onto the earth for determination of ground footprint geolocations. A similar result (not shown) was derived from the same information for TIRS2 except a small clocking error of 5 mrad is also discernible.

4.3. Optical Alignment—Spectral Calibration

Spectral calibration pre-flight measurements were made to support science algorithms in which accurate spectral response functions (SRFs) are required to model the spectral radiance measured by TIRS. The same GSE configuration for spatial calibration (see Supporting Information S1) was used. Details of the tests performed for each instrument (and configuration changes associated with the tests) are provided in the appendix. Tests were designed with variable integration times to accommodate differing levels of stimulus input and associated signal-to-noise ratios (SNR), tests were then inspected in near real-time and repeated if significant improvement in SNR was attainable within test time constraints.

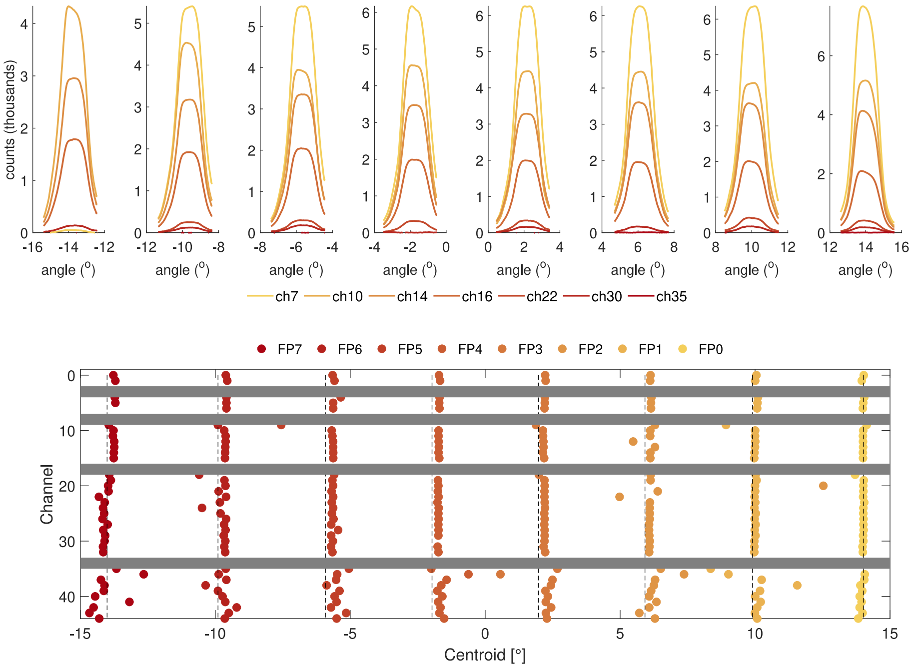

Figure 8. (top) Background subtracted, azimuth scans over TIRS1 scenes with broadband illumination (glowbar at roughly 800 K). (bottom) Centroids of broadband spatial scans of TIRS1 scenery (field points FP# are matched with scene numbering, sc#), with vertical dashed lines showing nominal design centroid values and gray bands indicating insensitive channels at filter boundaries. The low contrast from limited illumination at long wavelengths or from unresponsive pixels induces some scatter in the centroids.

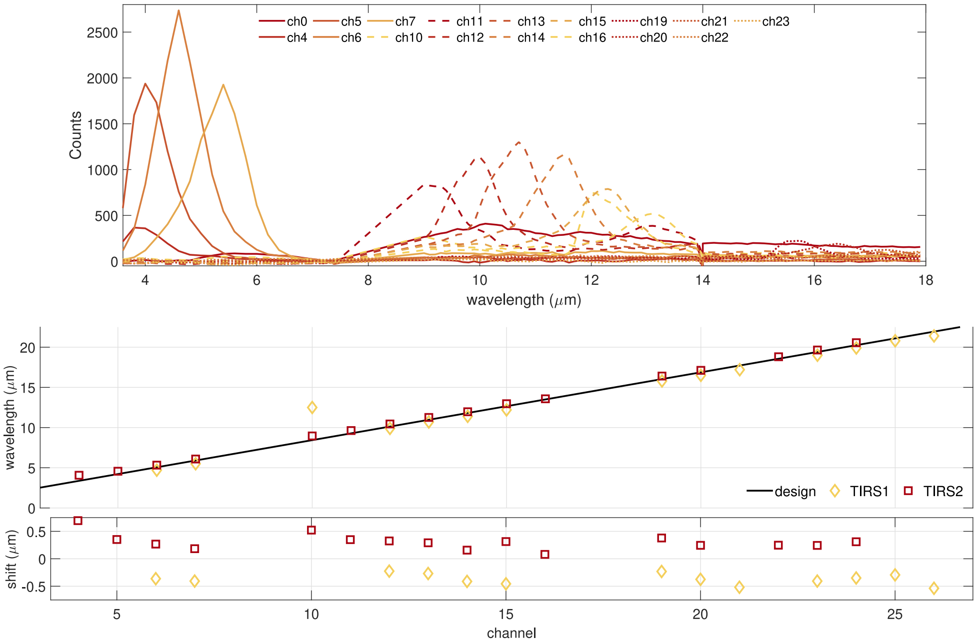

Figure 9. (upper) Background subtracted, sum of all scenes/field points, spectral scans of TIRS1. (middle) Measured spectral response centroids plotted with nominal design. (lower) Residual (difference of measured centroids and nominal design center wavelengths) versus channel for each TIRS.

Table 3
Instrument Geometry Model Parameters for Each TIRS

Parameter	Design	TIRS1	TIRS2	units
Δx	0	−90	115	microns
Δy	0	0	0	microns
Δz	0	0	0	microns
xy	0	0	−5	mrad
xz	0	0	0	mrad
yz	0	0	0	mrad
f_l	8.0	8.1	8.1	mm

Significant spectral shifts from nominal design were observed in both TIRS instruments, each in opposing spectral directions. The effects were quantified through determination of centroids in measured spectral responses for each pixel. Comparisons across scenes showed little variance outside of previously characterized bad pixels with limited or no response, this was consistent with the results of spatial calibration that showed a high degree of consistency across the spatially distinct scenery from each instrument. Given this uniformity, spectral scans from across all field points/scenes were co-added to produce the highest possible SNR for centroid determinations, these are shown in Figure 9 as differences from nominal design center wavelengths. For TIRS1 an offset of −0.4 μm (−90 microns in y coordinate of focal plane placement) is observed. For TIRS2 the spectral offset observed is +0.3 μm, suggesting an opposing shift of the focal plane placement. Table 3 summarizes the results of optimizing the instrument geometric model to match calibration data.

4.4. Radiometric and Environmental Testing

Environmental testing required for the TIRS instrumentation was performed in concert with radiometric calibrations utilizing a compact vacuum chamber equipped with temperature controllable radiometric targets as well as a heating/cooling table for control of instrument state (see Supporting Information S1 for a schematic and detailed listing of hardware).

The testing sequence cycled through instrument temperatures of 310, 262, 310, 317, 262, 294, 297, and 317 K, with the instrument operating in nominal “science” mode continuously with the exception of the periods at 317 K and immediately after. The extreme temperature ranges were chosen to satisfy flight hardware design principles for low-earth orbit conditions. During the instrument dwell period at 294 K, the warm radiometric target was stepped through six different temperatures, starting at 235K and increasing up to 310K in 15K increments. By flooding the fields of view with flat-field targets of known emissivity and temperature, many instrument design parameters can be tested with each radiometric measurement. Crucially, the fine alignment offsets associated with the elevation angle, TIRS pointing mirror, and the spectral wavelength, noted in the spatial/spectral calibration setup, are not realized, and any off-nominal shapes of the measured Planck curves are then useful for final determination of the spectral shifts. Each channel's calibrated response at its shifted central wavelength, is shown in Figure 10.

Noise equivalent difference temperatures (NEDT), determined for a 300 K blackbody, may be used to define the sensitivity of each TIRS. Figure 11 shows NEDT (single image precision) values derived from instrument data.

4.5. Combined Calibration Results

Collection of TIRS calibration data was time constrained due to budget driven delivery deadlines. Misalignments of the instruments were recognized in the course of measurements and the characterization efforts were deemed consistent with adjustable parameters within the instrument model. This model parameterizes the location of the focal plane with respect to the instrument slit while assuming the Offner system behaves ideally. Pixel positions in x,y (the nominal focal plane) as well as in the converging/diverging z coordinate of the nominally normal ray paths are defined by potential translations of x (spectral), y (spatial), z (focus) or potential rotations in xy (clocking), xz (tip), yz (tilt). The model convolves radiation geometrically defined by the slit width with the dispersion of the grating to account for diffraction and provide channel specific $\Re_{n,\lambda_i}$ values for determination of SRFs. An iterative process was used to explore off nominal values for the model that best reproduced all of the test data.

As described in Section 4.3 a −0.35 μm shift for TIRS1, was observed, however this shift was found to be inconsistent with the radiometric calibration data where the flat field radiances imply an additional −0.2 μm shift that was undetected in the spectral analysis due to ambiguity in the along track alignment. The total is consistent with a −90 micron shift of the focal plane in the optics x coordinate. A similar but larger alignment-related spectral shift is observed in TIRS2, resulting in an off-nominal x coordinate of +115 microns in the instrument model. The only other coordinate determined to be off-nominal is the clocking (xy rotation) of

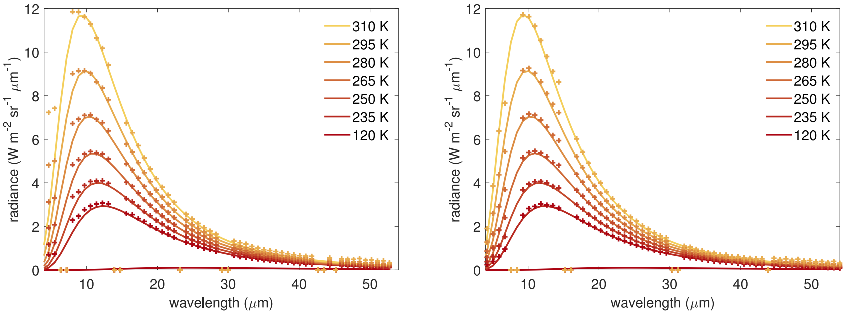

Figure 10. (left) Calibrated radiometric response for TIRS1 Scene 5. (right) Calibrated radiometric response for TIRS2 Scene 1.

TIRS2, which is observable in the broadband cross-track spatial scanning, the amount of clocking error is 5 mrad, which is within acceptance criteria, having a minimal effect on spatial uniformity in the spectral domain. With these corrections, the instrument model provides the spectral response functions (SRFs) shown in Figure 12.

Stray light associated with filter boundaries and ineffective order sorting due to small focal plane/filter misalignment is characterizable using all of the calibration data in tandem. The effects are noticeable at short wavelengths in TIRS1 (below 7 μm, peaking at 4 μm, see Figure 10). Interestingly, the short wave channels are sensitive to wavelengths in the filter 1/filter 2 gap around 8 μm, which could be of more scientific value than the relatively weak terrestrial emission at 4 μm. A significant challenge remains in characterizing the fields-of-view of this light, which may become a priority if the affected channels are shown to have useful science value.

Models for removing effects of stray light and electronics cross-talk have been formulated. These models may be optimized for each TIRS during the flight mission to allow for best effort removal of these effects from scene averages where the associated biases will be larger than the random noise.

4.6. Earth Observing

The TIRS instrument has a 1.3° cross-track and 3.3° along-track IFOV and is pointed nadir with the 8 spatial scenes falling discontinuously in a 28.3° swath. At nominal orbit ($H = 525$ km) the IFOV is 12×30 km^2. With a dwell time, t (the amount of time the image is integrated) the along-track instantaneous field of view, is dragged during the orbital motion. For $|V_g| = 7.6$ km/s a 82.1% overlap occurs in the prior and post samples and the integrated field of

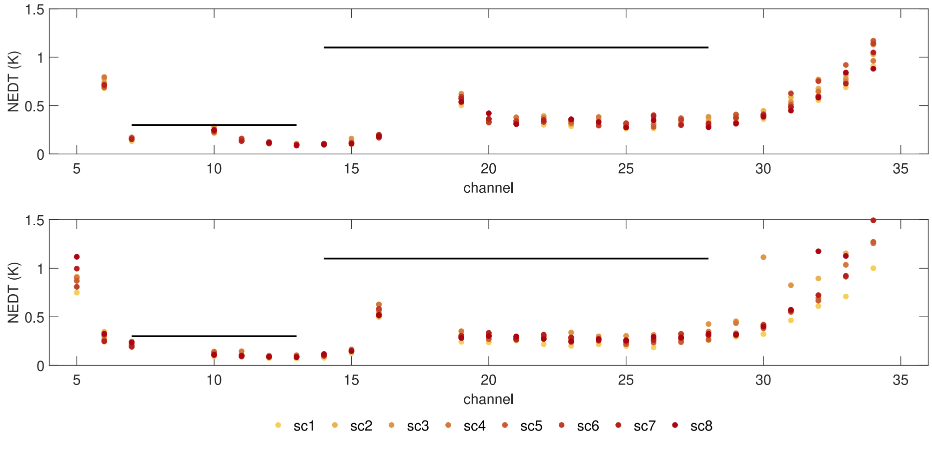

Figure 11. Noise equivalent difference temperatures associated with instrument noise ($\delta\mathbb{S}_{sc,n}$ and $\delta^x\mathbb{S}_{sc,n}$) for TIRS1 (upper) and TIRS2 (lower) from single image statistics. Instrument shortwave and longwave single image requirement values are shown as solid black lines. Temperature fluctuations in the orbital environment are expected to further reduce sensitivity and effects on NEDT will be re-assessed post-launch.

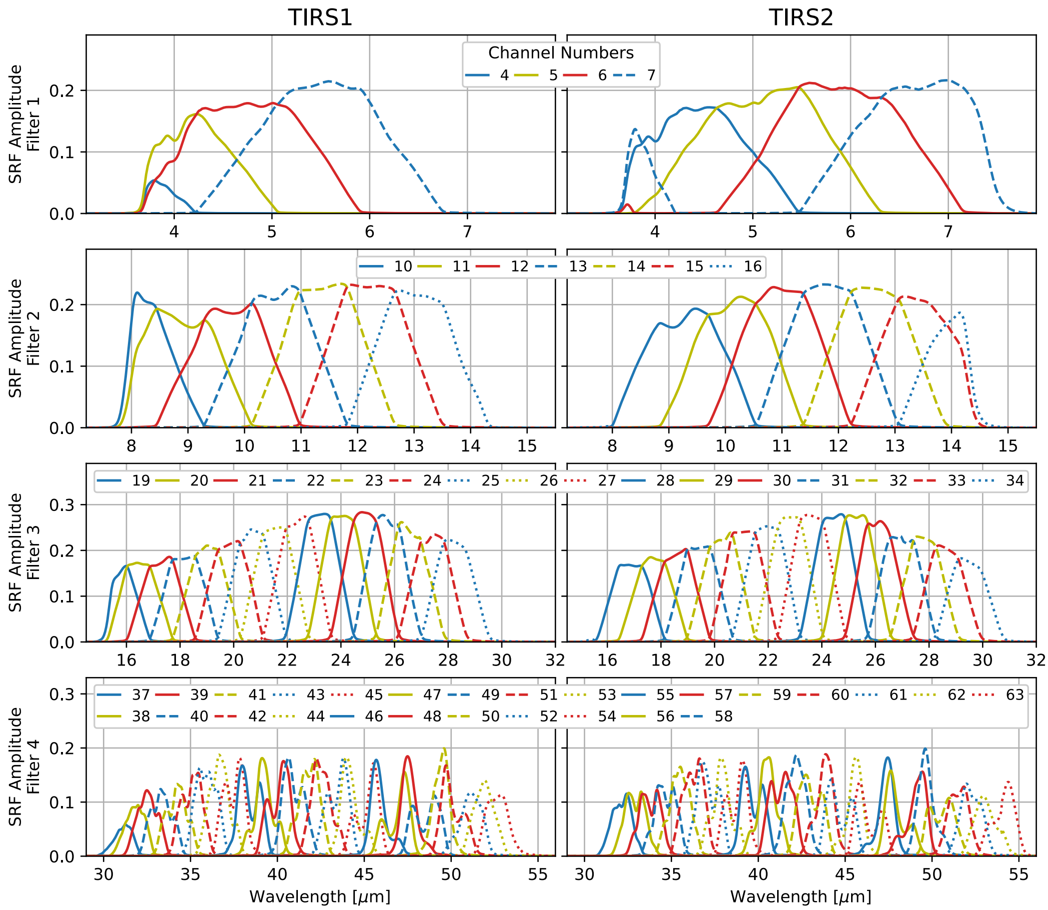

Figure 12. Spectral response functions (SRFs) for TIRS1 (left column) and TIRS2 (right column) as determined from the instrument models after reconcilation with test data. Each row displays the SRFs from one of the order-sorting filters. The pairs of channels not displayed are the sacrificed channels due to the order sorting filter edges (e.g., channels 8 and 9).

view is 12 × 36 km^2. Geolocation of TIRS imagery utilizes the instrument model's angular IFOV in concert with the CubeSat spacecraft attitude quaternion to first project out onto an oblate spheroid, then a refined, altitude corrected footprint is determined with line-of-sight corrections using the Copernicus GLO-90 DEM (ESA, 2022).

During in-orbit checkout, predictably sharp features in thermal imagery will be utilized to georectify the absolute pointing of each TIRS. Offset corrections to the CubeSat yaw/pitch/roll will be modified as necessary to reproduce observed thermal imagery with respect to known geographies.

4.7. Data Sufficiency and Measurement Uncertainty

In order to complete PREFIRE science objectives, the mission must acquire spectrally resolved thermal images of the seasonally varying Arctic. The instrument described, flying in polar orbit, enables this data record, however, the array format, the grating resolution, the telescope size, the CubeSat link budget and costs for downlink all constrain the amount of data available for science. The observing profile maximizes a diversity of scene types while collecting calibrated 5–54 μm spectral images over the Arctic and provides the data necessary to achieve baseline science objectives. Kahn et al. (2020) detail how surface type sampling characteristics can be met with fractions of the expected TIRS data. Level 2 data products for atmospheric state (Miller et al., 2023), surface temperature, surface emissivity (Yang et al., 2023), cloud fraction (Bertossa et al., 2023) and spectral flux (Xie et al., 2022) will systematically determine energy exchange processes that influence Arctic systems. These processes will be sampled by the PREFIRE mission over all relevant surface types, allowing for parameterized classification and subsequent injection into climate (Shaw & Kay, 2024) and process system driven models.

Table 4
TIRS Error Budgets and Performance Breakdowns, 6–11 μm

Error type	Symbol	Allocation	TIRS1[a]	TIRS2[a]
Instrument Noise (N)	$\delta\mathbb{S}_{sc,n}$	0.3 K	<0.7 K	<0.3 K
Instrument Noise (C/S)	$\delta^x\mathbb{S}_{sc,n}$	0.2 K	0.4 K	0.2 K
Emissivity model	$\delta^C I_{sc,n}$	0.4 K	<0.2 K	<0.1 K
Instrument Model	$\delta\eta_{sc,n}$	0.4 K	<0.7 K	<0.1 K
Instrument Stability[b]	$\delta^I\mathbb{S}_{sc,n}$	0.4 K	<0.4 K	<0.2 K
System Performance	NEDT	0.8–1.6 K	1.1–2.1 K	0.4–0.8 K

Note. See Supporting Information S1 for details. [a]Relative errors expressed in percentages in appendix are converted to NEDT biases by equating to random noise contributions by percentages within this spectral range. [b]Instrument stability is currently determined under relatively ideal conditions (radiative calibration setup) over a relatively short time period, this will be re-evaluated on-orbit throughout the mission.

Data quality is determined by a combination of instrument performance, spacecraft pointing and spacecraft temperature stability. Spacecraft pointing and thermal characteristics are expected to be manageable and will be evaluated in a post-launch performance characterization, here we provide a summary of the ground characterization of the instrument, for details, see the Supporting Information S1.

The instrument noise and biases associated with unknowns in materials properties or model parameters are derived using the theoretical basis given in Section 2 and are presented here as worst cases for good channels, that is, for channels with $D^* > 5 \times 10^8$ Jones (see Figure 2) that will be calibrated in level 1 algorithms. Tables 4 and 5 show the design allocations and instrument specific error contributions for the shortwave channels of each TIRS. The total system performance NEDT values are the component sums in quadrature (lower bound, best case) and with systematic errors summed linearly (upper bound, worst case).

The first rows of Tables 4 and 5 describe random noise in TIRS Nadir (N) imagery. The entries are simplified representations of Figure 11, where it can be seen that the excedance of the instrument noise allocation in TIRS1 was for the shortest wavelength channel in the range ($n = 7$). The science team evaluated the impact of this additional noise and determined that the associated information regarding atmospheric humidity could be adequately retrieved from the prevalence of less sensitive long-wavelength channels, allowing for acceptance of this performance issue.

The second rows of these tables are logical extensions of the first row and account for random noise propagated into TIRS nadir imagery upon calibration. Details of the error propagation can be found in Supporting Information S1.

The last three rows of Tables 4 and 5 are the most important, as they describe the bias associated with unknowns in the TIRS calibration model and its stability. In high accuracy climate missions, small errors in the instrument calibration can result in significant biases in global variables and/or long term trends, however, PREFIRE is designed to focus on specific regions and processes where the associated radiative signals have large (but poorly characterized) contrasts. The entire error budget was designed to meet science requirements associated with characterizing spectral contrasts within scenes. The relatively small TIRS random error components indicate that the signals will surely be observed. Biases are channel dependent and constrained by the characterizations described. These together will provide uncertainty estimates of the spectral radiance products.

Table 5
TIRS Error Budgets and Performance Breakdowns, 12–24 μm

Error type	Symbol	Allocation	TIRS1[a]	TIRS2[a]
Instrument Noise (N)	$\delta\mathbb{S}_{sc,n}$	1.4 K	<0.6 K	<0.6 K
Instrument Noise (C/S)	$\delta^x\mathbb{S}_{sc,n}$	0.8 K	0.3 K	0.3 K
Emissivity model	$\delta^C I_{sc,n}$	0.4 K	<0.2 K	<0.2 K
Instrument Model	$\delta\eta_{sc,n}$	0.4 K	<0.2 K	<0.2 K
Instrument Stability[b]	$\delta^I\mathbb{S}_{sc,n}$	0.4 K	<0.3 K	<0.3 K
System Performance	NEDT	1.8–2.8 K	0.8–1.4 K	0.8–1.4 K

Note. See Supporting Information S1 for details. [a]Relative errors expressed in percentages in appendix are converted to NEDT biases by equating to random noise contributions by percentages within this spectral range. [b]Instrument stability is currently determined under relatively ideal conditions (radiative calibration setup) over a relatively short time period, this will be re-evaluated on-orbit throughout the mission.

In both TIRS instruments, the internal calibration target was shown (see Supporting Information S1) to behave ideally over short periods (hours), and the estimates of just how well the internal calibration can be trusted are limited by analysis effort. This effort may be revisited if other likely sources of calibration error (discussed next) are not limiting factors.

The second last row in Tables 4 and 5 describes knowledge of the channel-specific instrument throughput, note that we define a channel optical efficiency as $\eta_{sc,n} = \Sigma SRF_{sc,n}/N$. This error component is very challenging to quantify (see Supporting Information S1, both from the scientific requirement standpoints as well as from the engineering verification standpoint. As defined here, it is an optical efficiency related to a specified *unshifted* spectral range. Since the TIRS systems exhibited spectral shifts, the values are mostly self-compensating (one channel picks up what its neighbor lost), up until a filter boundary. Lost efficiency near filter boundaries are worst for TIRS1 at short-wavelengths, where the desired information content of $n = 7$ is near zero. For related reasons, the random noise in this channel is also higher. Technically, the retrieval of science data depends on the shape of the SRF as well as the total efficiency of a channel. Based on the limited signal to noise ratio of the system-level spectral calibration data, it was decided to use the component characterization data to fix these shapes. This assumption works well in a pure radiometric sense across most of the TIRS bandwidth, with notable exceptions at short wavelengths in TIRS1, as shown in Figure 10. The assumption would likely be circumspect for study of narrow-band (unresolved) spectral features.

Finally, the TIRS instruments measure image radiance as a difference from the instrument radiance, meaning that any uncalibrated fluctations in instrument temperature appear as noise in imagery. The thermal model discussed in Section 3.7 provides for the estimate given in the last rows of Tables 4 and 5, but this contribution will be re-evaluated on-orbit with initial extra calibration cycles to flesh out any idiosyncracies of the instrument thermal profile. It is also possible that instrument components may have time-dependent properties, such as detector responsivity and filter or paint reflectivity, so we plan to carefully monitor instrument and calibration stability over the length of the flight project.

5. Conclusions

In this paper we have described the design, function and performance of thermal infrared spectrometers capable of making representative spectral far-infrared measurements of the majority of the Earth's polar radiation for NASAs PREFIRE project. Adherence to NASA and JPL design principles, balanced with cost and time saving system trades, resulted in the project being poised to make novel measurements to address scientific hypotheses regarding the rapidly changing climate. Though novel, the radiometric methods and spectrometric techniques trace to proven hardware and sound theory and are shown to have acceptable performance.

Acknowledgments
The authors would like to thank conceptual support from Graeme Stephens, Thomas Pagano, David Ryder and Joshua Fisher. TIRS designs and analysis was supported by Sharmila Padmanabhan, Mary White, James McGuire, Dan Wilson, Omar De Santos, Andrew Houck, Eric Hochberg, Yuri Bergovski, Scott Ellis (Photon Engineering), David Martinez, Lori Moore, Bruce Cameron, Rudi Bendig, Matt Kenyon, Giacomo Mariani, Byongho Eom, Ian McKinley, Rogelio Rosas and Harrison Bird. TIRS assembly was performed by Sharmila Padmanabhan, Rudi Bendig, Ryan White, Byongho Eom, Matt Kenyon, Marc Foote, Harrison Bird, Harrison Herzog, David Aldrich, Heather Lim and Ian McKinley. Ground support equipment was developed by Brian Drouin, Rachel Weinberg/Kenney, Deacon Nemchick, Jeffrey Hein, Eric Hochberg, Marc Foote, Harrison Herzog, Rudi Bendig, David Martinez, Tim Crawford and Lavanya Periasamy. Ground support equipment software was developed by Jason Matthews, Michael McKee, and Jeffrey Hein. Instrument science algorithms were developed by Brian Drouin, Erin Hokanson Wagner, Tim Michaels and Aronne Merrelli. Hardware testing was performed by Sharmila Padmanabhan, Marc Foote, Brian Drouin, Deacon Nemchick, Mary White, David Martinez, Rudi Bendig, Ian McKinley, Harrison Herzog, David Aldrich, Heather Lim, Robert Smythe, Arthur Na-Nakornpanom, Oscar Deng, Rogelio Rosas, Dean Johnson, Fabien Nicaise, Peter Ringold and Kyra Shanks. Safety and mission assurance was provided by Carlo Abesamis, Cesar Amaro, William Jones-Wilson and Michael Robinson. Contributions of Tristan L'Ecuyer and Aronne Merrelii were supported under NASA PREFIRE Grant 80NSSC18K148. Portions of this research were performed at the Jet Propulsion Laboratory, California Institute of Technology, under contract with the National Aeronautics and Space Administration. ©2024.

Data Availability Statement

The Supporting data described in the manuscript is available at the journal and Supporting Information S1 is available as a zip file containing the datafiles and metadata description, are at JPL Open repository (B. Drouin, 2024) Dataverse.

References

Atmospheric Science Data Center. (n.d.). https://doi.org/10.5067/PREFIRE-SAT2/PREFIRE/RAD_L1B.R00

Bertossa, C., L'Ecuyer, T., Merrelli, A., Huang, X., & Chen, X. (2023). A neural network-based cloud mask for PREFIRE and evaluation with simulated observations. *Journal of Atmospheric and Oceanic Technology*, *40*(4), 377–396. https://doi.org/10.1175/JTECH-D-22-0023.1

Blanchet, J.-P., Royer, A., Châteauneuf, F., Bouzid, Y., Blanchard, Y., Hamel, J.-F., et al. (2011). TICFIRE: A far infrared payload to monitor the evolution of thin ice clouds. In R. Meynart, S. P. Neeck, & H. Shimoda (Eds.), *Sensors, Systems, and Next-Generation Satellites XV* (Vol. 8176, p. 81761K). SPIE. https://doi.org/10.1117/12.898577

Drouin, B. (2024). Thermal infrared spectrometers for the polar radiant energy in the far-infrared experiment (PREFIRE), supplemental data description [Dataset]. https://doi.org/10.48577/jpl.THYA8I

Drouin, B. J., Kahn, B., Lim, B., Merrelli, A., Nelson, E., Quinn, G., et al. (2022). Orbital trade study for the PREFIRE mission. In *2022 IEEE Aerospace Conference (AERO)* (pp. 1–7). https://doi.org/10.1109/AERO53065.2022.9843312

ESA. (2022). Copernicus DEM—Global and European digital elevation model (COP-DEM). https://doi.org/10.5270/ESA-c5d3d65

Fisher, J. B., Lee, B., Purdy, A. J., Halverson, G. H., Dohlen, M. B., Cawse-Nicholson, K., et al. (2020). ECOSTRESS: NASA's next generation mission to measure evapotranspiration from the international space station. *Water Resources Research*, *56*(4), e2019WR026058. https://doi.org/10.1029/2019WR026058

Green, R. O., Pieters, C., Mouroulis, P., Eastwood, M., Boardman, J., Glavich, T., et al. (2011). The Moon Mineralogy Mapper (M3) imaging spectrometer for lunar science: Instrument description, calibration, on-orbit measurements, science data calibration and on-orbit validation. *Journal of Geophysical Research*, *116*, E00G19. https://doi.org/10.1029/2011JE003797

Henderson, G. R., Barrett, B. S., Wachowicz, L. J., Mattingly, K. S., Preece, J. R., & Mote, T. L. (2021). Local and remote atmospheric circulation drivers of arctic change: A review. *Frontiers in Earth Science*, *9*, 709896. https://doi.org/10.3389/feart.2021.709896

Hulley, G. C., Duren, R. M., Hopkins, F. M., Hook, S. J., Vance, N., Guillevic, P., et al. (2016). High spatial resolution imaging of methane and other trace gases with the airborne hyperspectral thermal emission spectrometer (HyTES). *Atmospheric Measurement Techniques*, *9*(5), 2393–2408. https://doi.org/10.5194/amt-9-2393-2016

Hwang, Y.-T., Frierson, D. M. W., & Kay, J. E. (2011). Coupling between arctic feedbacks and changes in poleward energy transport. *Geophysical Research Letters*, *38*(17). https://doi.org/10.1029/2011GL048546

Kahn, B. H., Drouin, B. J., & L'Ecuyer, T. S. (2020). Assessment of sampling sufficiency for low-cost satellite missions: Application to PREFIRE. *Journal of Atmospheric and Oceanic Technology*, *37*(12), 2283–2298. https://doi.org/10.1175/JTECH-D-20-0023.1

L'Ecuyer, T. S., Drouin, B. J., Anheuser, J., Grames, M., Henderson, D. S., Huang, X., et al. (2021). The polar radiant energy in the far infrared experiment: A new perspective on polar longwave energy exchanges. *Bulletin of the American Meteorological Society*, *102*(7), E1431–E1449. https://doi.org/10.1175/BAMS-D-20-0155.1

Mariani, G., & Kenyon, M. (2015). Room-temperature remote sensing: Far-infrared imaging based on thermopile technology. In *2015 40th International Conference on Infrared, Millimeter, and Terahertz waves (IRMMW-THz)* (pp. 1–2). https://doi.org/10.1109/IRMMW-THz.2015.7327704

Mariani, G., Kenyon, M., Eom, B., Drouin, B., & White, M. (2019). Far-infrared room-temperature focal plane modules for polar radiant energy in the far infrared experiment. In *2019 44th International Conference on Infrared, Millimeter, and Terahertz waves (IRMMW-THz)* (pp. 1–2). https://doi.org/10.1109/IRMMW-THz.2019.8877588

McCleese, D. J., Schofield, J. T., Taylor, F. W., Calcutt, S. B., Foote, M. C., Kass, D. M., et al. (2007). Mars climate sounder: An investigation of thermal and water vapor structure, dust and condensate distributions in the atmosphere, and energy balance of the polar regions. *Journal of Geophysical Research*, *112*(E5). https://doi.org/10.1029/2006JE002790

McKinley, I. M., Allen, G. D., Rosas, R., & Andrade, A. (2022). Thermal design of the thermal infrared spectrometer (TIRS) instrument on PREFIRE. In *2022 IEEE Aerospace Conference (AERO)* (pp. 1–9). https://doi.org/10.1109/AERO53065.2022.9843559

Miller, N. B., Merrelli, A., L'Ecuyer, T. S., & Drouin, B. J. (2023). Simulated clear-sky water vapor and temperature retrievals from PREFIRE measurements. *Journal of Atmospheric and Oceanic Technology*, *40*(6), 645–659. https://doi.org/10.1175/JTECH-D-22-0128.1

Mouroulis, P., Hartley, F., Wilson, D., White, V., Shori, A., Nguyen, S., et al. (2003). Blazed grating fabrication through gray-scale x-ray lithography. *Optics Express*, *11*(3), 270–281. https://doi.org/10.1364/OE.11.000270

Mouroulis, P., Wilson, D., Maker, P., & Muller, R. (1998). Convex grating types for concentric imaging spectrometers. *Applied Optics*, *37*(31), 7200–7208. https://doi.org/10.1364/AO.37.007200

Padmanabhan, S., Drouin, B., L'Ecuyer, T., White, M., Lim, B., Kenyon, M., et al. (2019). The polar radient energy in the far infrared experiment (PREFIRE). In *IGARSS 2019—2019 IEEE International Geoscience and Remote Sensing Symposium* (pp. 8834–8836). https://doi.org/10.1109/IGARSS.2019.8899259

Paige, D. A., Foote, M. C., Greenhagen, B. T., Schofield, J. T., Calcutt, S., Vasavada, A. R., et al. (2010). The lunar reconnaissance orbiter diviner lunar radiometer experiment. *Space Science Reviews*, *150*(1–4), 125–160. https://doi.org/10.1007/s11214-009-9529-2

Peterson, C. A., Chen, X., Yue, Q., & Huang, X. (2019). The spectral dimension of arctic outgoing longwave radiation and greenhouse efficiency trends from 2003 to 2016. *Journal of Geophysical Research-Atmospheres*, *124*(15), 8467–8480. https://doi.org/10.1029/2019JD030428

Prieto-Blanco, X., Montero-Orille, C., Couce, B., & de la Fuente, R. (2006). Analytical design of an Offner imaging spectrometer. *Optics Express*, *14*(20), 9156–9168. https://doi.org/10.1364/OE.14.009156

Seeley, J., Hunneman, R., & Whatley, A. (1979). Infrared multilayer interference filter manufacture—Supposed longwave limit. *Applied Optics*, *18*(20), 3368–3370. https://doi.org/10.1364/AO.18.003368

Shaw, J. K., & Kay, J. E. (2024). Processes controlling the seasonally varying emergence of forced arctic longwave radiation changes. *Journal of Climate*, *36*(20), 7337–7354. https://doi.org/10.1175/jcli-d-23-0020.1

Van Gorp, B., Mouroulis, P., Blaney, D., Green, R. O., Ehlmann, B. L., & Rodriguez, J. I. (2014). Ultra-compact imaging spectrometer for remote, in situ, and microscopic planetary mineralogy. *Journal of Applied Remote Sensing*, *8*(1), 084988. https://doi.org/10.1117/1.JRS.8.084988

Wielicki, B. A., Young, D. F., Mlynczak, M. G., Thome, K. J., Leroy, S., Corliss, J., et al. (2013). Achieving climate change absolute accuracy in orbit. *Bulletin of the American Meteorological Society*, *94*(10), 1519–1539. https://doi.org/10.1175/BAMS-D-12-00149.1

Xie, Y., Huang, X., Chen, X., L'Ecuyer, T. S., & Drouin, B. J. (2023). Joint use of far-infrared and mid-infrared observation for sounding retrievals: Learning from the past for upcoming far-infrared missions. *Earth and Space Science*, *10*(3), e2022EA002684. https://doi.org/10.1029/2022EA002684

Xie, Y., Huang, X., Chen, X., L'Ecuyer, T. S., Drouin, B. J., & Wang, J. (2022). Retrieval of surface spectral emissivity in polar regions based on the optimal estimation method. *Journal of Geophysical Research-Atmospheres*, *127*(5), e2021JD035677. https://doi.org/10.1029/2021JD035677

Yang, Z., Chen, X., Huang, X., L'Ecuyer, T., & Drouin, B. (2023). A fast neural network-based approach for joint mid-IR and far-IR surface spectral emissivity retrieval. In *IGARSS 2023–2023 IEEE International Geoscience and Remote Sensing Symposium* (pp. 5324–5327). https://doi.org/10.1109/IGARSS52108.2023.10281903

Zmuidzinas, J. (2012). Superconducting microresonators: Physics and applications. In J. Langer (Ed.), *Annual Review of Condensed Matter Physics* (Vol. 3, pp. 169–214). https://doi.org/10.1146/annurev-conmatphys-020911-125022